Tech Science Press

Multi-Band Bandpass Filter Using Novel Topology for Next-Generation IoT Wireless Systems

Muhammad Faisal* and Sohail Khalid

Departmnet of Electrical Engineering, Riphah International University, Islamabad, 44000, Pakistan
*Corresponding Author: Muhammad Faisal. Email: muhammad.faisal@riphah.edu.pk

Abstract: The design of single- and quad-band Bandpass Filter (BPF) topology has been presented in this paper for next-generation Internet of Things (IoT) devices. The main topology is constructed using the Split Ring Resonator (SRR), separated by the Anti-Parallel Coupled Line Structure (APCLS). A detailed analysis of APCLS has been presented, which is further used to construct the single- and quad-band BPF. The single-band BPF design consists of SRR loaded with APCLS. The developed single-band BPF displays a dual-mode response with a center frequency of 2.65 GHz and a measured fractional bandwidth of 17.17%. Moreover, a quad-band bandpass filter has been achieved using the same topology with minor modification in the SRR and APCLS electrical parameters. The developed quad-band BPF generates a dual-mode response having center frequencies of 1.2, 2.4, 3.5, and 4.7 GHz with the measured fractional bandwidth of 13%, 26%, 16%, and 5%, respectively. Two prototypes have been fabricated on the high-frequency substrate to validate the proposed topologies. Very high rejection in the stopbands region, little in-band insertion loss, and very selective passband have been measured for single- and quad-band BPFs. The measured and simulated results are well correlated.

Keywords: Single-band BPF; quad-band BPF; anti-parallel coupled line structure; split ring resonator; internet of things

1 Introduction

Modern IoT wireless communication systems, like Bluetooth, Zonal Intercommunication Global-standard (ZigBee), Long Range Radio (LoRa), NarrowBand (NB)-IoT, and Wireless Fidelity (WiFi) demand multiband frequency response. Moreover, the IoT wireless communication nodes required low-powered miniaturized designed components. Therefore, the RF front end of an IoT device must have a compact design while maintaining good electrical performance. Over the last few years, many researchers have provided the design topologies of single and multiband BPF for low-powered compact IoT devices. In [1], the proposed structure involves two sections of three-quarter wavelength coupled lines separated by a non-uniform transmission line to obtain a wideband BPF

filter response. Moreover, a dual-path structure that involves an inter-digital coupled line in parallel with the transmission line is presented in [2] to realize a wide BPF response. Another coupled step impedance resonator (SIR) technique in [3] is used to realize the single and dual-band BPF response. The measured result shows little discrepancies at the upper stopband for both single and dual BPF filters. Furthermore, three pairs of coupled lines structures and two pairs of transmission lines are integrated in such a way to obtain a highly selective BPF response [4]. The ideal response consists of eight transmission zeros (TZs) and five transmission poles (TPs) within the 2fc; however, the microstrip and fabricated results show less TZs at the upper stopband. The cross-shaped resonator having three coupled line structures is integrated to achieve the wide BPF filter response [5]. The resonator having a parallel-coupled line as feed is replaced with three coupled line feed to achieve strong coupling that helped in obtaining better out of band rejection and reducing the return loss in the passband.

The wide BPF response using the ring embedded ring resonator technique is realized in [6]. The embedded rings helped reduce the size of the filter and produce a wider upper stopband. However, the measured result shows high discrepancies in the upper stopband region compared to the simulated results. The structure having two coupled SIR and a ring resonator in the ground plane is implemented to achieve a better wide BSF response [7]. The presence of the ring resonator in the ground plane enhanced the coupling of the overall structure and extracted a better passband response. The Stub-loaded Square ring resonator technique achieves single and dual-band BPF response [8]. A single BPF response is obtained by implementing a simple stub-loaded square ring resonator separated by an interdigital coupled line feed. Whereas the dual BPF response is achieved using two stub-loaded square ring resonators in the overall structure separated through coupled feeds. The measured result for the dual-band BPF filter shows high discrepancies in the upper passband compared to the simulated result.

Over the last decade, multi-band BPFs have gained popularity in multi-band IoT wireless communication systems. Substantial research has been done on dual- and tri-band BPFs. Nowadays, researchers are more focused on developing miniaturized quad-, penta-, and sext-band BPFs. Different design topologies have been adopted to develop quad-band BPF [9–23]. A popular method to design a quad-band BPF is by using stub-loaded topology [9–13]. In [9], a quad-band BPF with only three finite frequency transmission zeros using symmetrical stub-loaded topology has been presented. The two upper passbands measured insertion loss is not up to the mark. Two open-ended stubs resonators are loaded at the center of the two outer resonators [10] to achieve a quad-band BPF response. High discrepancies between the simulated and measured results have been noted for the upper passbands. A multi-stub-loaded resonator is presented in [11] to obtain a quad-band BPF response. Different stubs configurations can independently control the frequencies. However, each band's insertion loss and selectivity are not good enough. In [12], another quad-band BPF has been presented using a stub-loaded resonator. The even and odd mode method is used to analyze the symmetrical structure. However, the insertion loss is very high for each passband; moreover, the return loss is not up to the mark. Additionally, the quad-band BPF response has been realized using the multi-section stub-loaded resonators [13]. Five transmission zeros have been obtained around the passband to enhance the selectivity, whereas the insertion loss is quite high for each passband. Moreover, the SIR topology has been utilized to obtain quad-band BPF response [14,15,20]. In [14], open-circuited SIR loaded with short-circuited stubs is utilized to realize the quad-band BPF response with three transmission zeros across the four passbands. The overall size of the circuit is compact, but the insertion loss is above 2.3 dB. A triangular loop open-circuited stub-loaded SIR is implemented to achieve a quad-band BPF response [20]. The return loss is quite better, having six transmission zeros for better selectivity and isolation, but the insertion loss is bad. Moreover, the step impedance ring resonator (SIRR) topology is reported in [21] to obtain quad-band BPFs. The input/output coupled line structure is implemented

with the SIRR to generate four passbands. However, the insertion loss in the upper three passbands is quite high.

In this paper, the single- and quad-band BPF is designed using the SRR loaded with the APCLS. At first, the single-band BPF is designed using the proposed topology; afterward, little modification in the electrical parameters of the topology is performed to obtain the quad-band BPF response. The accomplished single- and quad-band BPF provides a dual-mode response with good electrical performance having higher out-of-band rejection and selectivity. A total of three and seven finite frequency transmission zeros are achieved for single and quad-band BPF filters, respectively. The finite frequency transmission zeros and the band of both the filters can be controlled through the variation in the dimensions of the SRR and APCLS. The prototypes are fabricated on RT/Duroid 5880 with a relative dielectric constant of 2.2. The selected substrate is low-powered and rugged, providing a suitable integration in a wireless IoT node RF front end. The measured results show good agreement with the simulated results for both filters.

2 Design Methodology

Fig. 1 displays the ideal topology of the proposed single- and quad-band BPF. The topology consists of a split ring resonator separated through the anti-parallel coupled line structure.
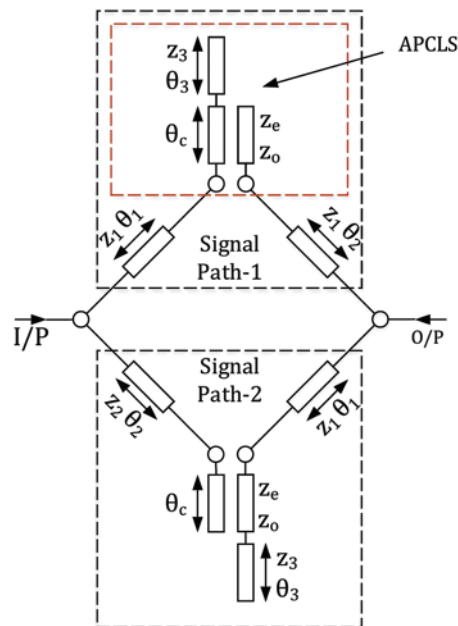

Figure 1: Ideal topology of SRR loaded with APCLS

Four transmission lines that are part of SRR have the characteristic impedance of Z_1, Z_2 and the electrical length of θ_1, θ_2 are connected with the APCLS. In order to extract the scattering parameter of the overall structure, the analysis of the APCLS should be conducted first. The proposed APCLS is shown in Fig. 2.

2.1 Proposed Anti-parallel Coupled Line Structure

The APCLS is developed using the parallel-coupled line with the even and odd impedances Z_e, Z_o and the electrical length θ_c embedded at port 3 with an open-circuited stub that has the characteristic impedance of Z_3 and electrical length of θ_3.
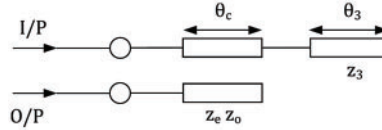
Figure 2: Proposed anti-parallel coupled line structure

In [24], the transfer matrix of the parallel-coupled line structure has already been discussed and concluded in the form of equations Eqs. (1) and (2).

$$[T]_o = \begin{bmatrix} \cos\theta_o & jZ_o\sin\theta_o \\ \dfrac{j\sin\theta_o}{Z_o} & \cos\theta_o \end{bmatrix} \tag{1}$$

$$[T]_e = \begin{bmatrix} \cos\theta_e & jZ_e\sin\theta_e \\ \dfrac{j\sin\theta_e}{Z_e} & \cos\theta_e \end{bmatrix} \tag{2}$$

An extra load at port 3 of the parallel-coupled line structure can be expressed in the form of an open-circuited stub as given in Eq. (3).

$$[T]_2 = \begin{bmatrix} 1 & -jZ_3\cot\theta_3 \\ 0 & 1 \end{bmatrix} \tag{3}$$

The electrical length $\theta_1 = \theta_2 = \theta_3 = \theta$ is suggested for calculation, the S-parameter response shown in Fig. 3a is plotted using Eq. (4). To validate the theoretical response, an ideal APCLS is designed and simulated while keeping the center frequency of 1 GHz. Fig. 3b shows the simulated response, which is well correlated with the theoretical response. Moreover, the electrical length and frequency conversion formula is $\theta = \dfrac{2\pi * f * l}{c}$, where l is the actual length of the transmission line, and c is the speed of light.

$$|S_{12}| = \frac{2}{\sqrt{a+b}} \tag{4}$$

where,

$$a = \frac{\{8z_3\,(z_e+z_o)\}\cos^3\theta + \{8z_ez_o - 4\sin^2\theta\,(z_e+z_o)^2\}\cos\theta}{[z_e+z_o][\{4z_3\}\cos^3\theta - \{2\sin^2\theta\,(z_e+z_o)\}\cos\theta]}$$

$$b = [\{-8z_3z_ez_o\}\cos^5\theta + \{4\sin^2\theta\,(z_e+z_o)\,z_ez_o + 8z_3\sin^2\theta\}\cos^3\theta + \{-4\sin^4\theta\,(z_e+z_o)$$

$$+ 4\sin^2\theta\,(z_e+z_o)\}\cos\theta] \times [\{z_e-z_o\}\{(4z_3\sin\theta)\cos^3\theta - (2\sin^3\theta\,(z_e+z_o))\cos\theta\}]^{-1}$$
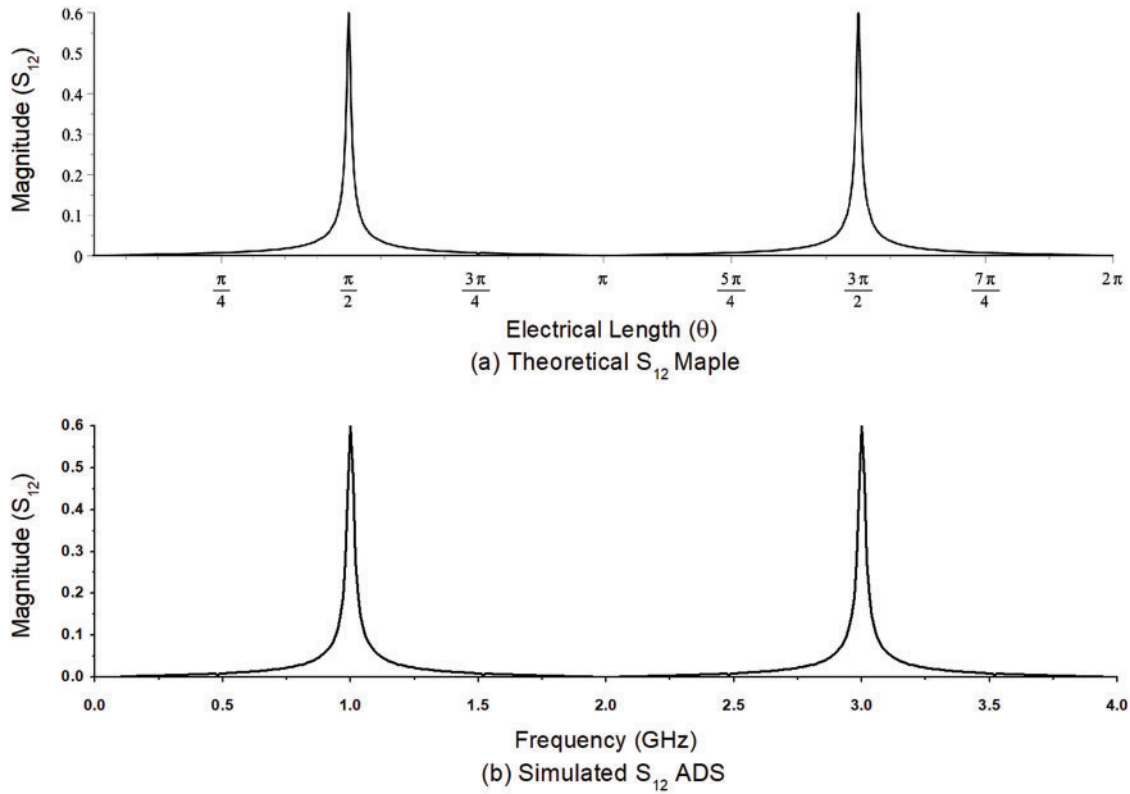
Figure 3: Comparison of theoretical and simulated response of APCLS

2.2 Proposed Single-Band BPF Filter

The proposed single-band BPF filter is constructed using the SRR loaded with the APCLS. The transfer matrix of the anti-parallel coupled line structure is already being extracted. It can be observed from Fig. 1 that the path 1 and path 2 are in parallel; therefore, the extracted transfer matrix of path 1, and path 2 is converted into their respective admittance matrix. The addition is performed on the admittance matrix of both paths to calculate the final admittance matrix. Afterward, the final admittance matrix is converted back into the transfer matrix to calculate the scattering parameter given in Eq. (5). To avoid complexity the impedances $Z_1 = Z_2$ and the electrical length $\theta_1 = \theta_2$ is recommended for calculations.

$$|S_{12}| = \frac{-2\alpha}{Zo\left(\frac{\beta}{Zo} + \gamma\right)^2 - \delta^2} \tag{5}$$

where,

$$\alpha = j\{(-2\varepsilon_1)\sigma\}\beta$$

$$\beta = \{2z_1 \sin^2\theta_1\}\{-\varepsilon_1^2 + 2\varepsilon_1 + \varepsilon_2^2\}\sigma - \{2\cos^2\theta_1\}\sigma + \{z_1 \sin 2\theta_1\}$$

$$\{(\varepsilon_1)\sigma - 4\}$$

$$\gamma = j\{2 \sin 2\theta_1\}\{-z_1\varepsilon_2^2 + z_1\varepsilon_1^2 - 2\varepsilon_1 - \frac{1}{z_1}\}\sigma + j\{8 - (\varepsilon_1)\sigma\}$$

$$\delta = j\{-2\varepsilon_1\}\sigma$$

The values of ε_1, ε_2, and σ are as follows:

$$\varepsilon_1 = \frac{(z_e + z_o)\sin\theta}{z_e z_o \cos\theta}, \quad \varepsilon_2 = \frac{(z_o - z_e)\sin\theta}{z_e z_o \cos\theta},$$

$$\sigma = \frac{\sin 2\theta (z_e + z_o)\sin\theta_3 - 4z_3 \cos^2\theta \cos\theta_3}{\sin\theta_3}$$

By using the synthesis procedure opted in [25,26], the coefficient values are extracted. Furthermore, the electrical parameters of the single-band bandpass filter shown in Fig. 4 are calculated using the coefficient values. The obtained electrical parameter values are $Z_{in} = 152.16$, $\theta_{in} = 0.83$, $Z_1 = Z_2$ = 84.71 Ω, $\theta_1 = \theta_2 = 44.26$, $Z_e = 70.85$ Ω, $Z_o = 18.75$ Ω, $\theta_c = 10$, $Z_s = 17.03$ Ω, $\theta_s = 14.54$. The ideal results of the proposed filter is given in Fig. 5, it can be seen that the two transmission poles are realized at $f_1 = 2.52$ GHz and $f_2 = 2.79$ GHz. Moreover, there are three finite frequency transmission zeros located at 1.9, 3.4, and 6.7 GHz, respectively.
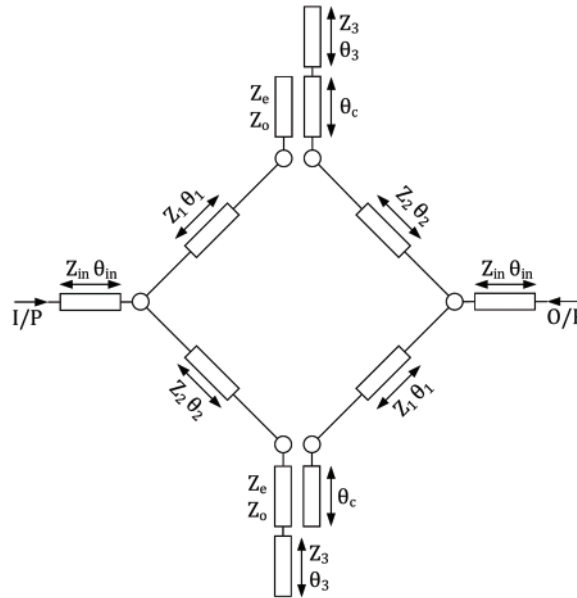

Figure 4: Ideal design of the proposed single-band BPF

Through detailed analysis, it has been observed that the finite frequency transmission zeros are controlled by the electrical length of SRR and APCLS. To provide the evidence, Fig. 6 shows the tuning of transmission zeros. Fig. 6a reveals that by increasing the electrical length θ_1 only the TZ_2 is changing and moving towards the lower frequency. The same kind of performance is observed for the case of TZ_1 as shown in Fig. 6b. In actual fact, the TZ_1 and TZ_2 is dependent and determined by the transmission lines of SRR having an electrical length of θ_1 and θ_2.

Similarly, with the variation in the electrical length θ_3 it has been observed from Fig. 6c that the TZ_1, and TZ_3 is showing some deviations, however the TZ_2 is not. This clearly indicates that the TZ_2 is independent of the electrical length θ_3. Moreover, the electrical length of coupled line structure θ_c is involved in the band shifting, as can be seen from Fig. 6d.
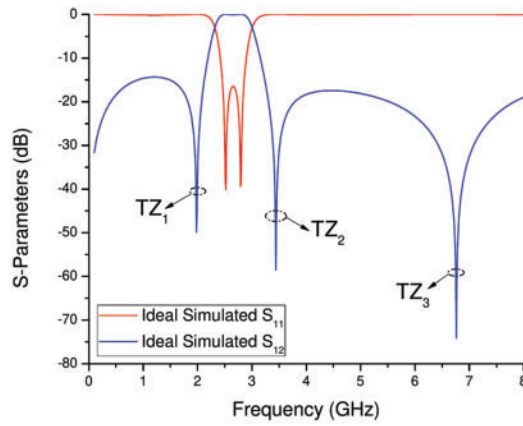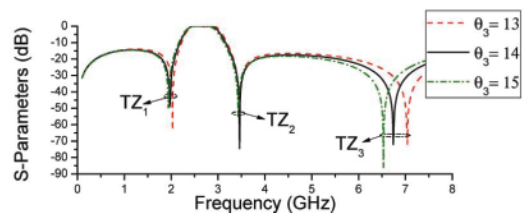
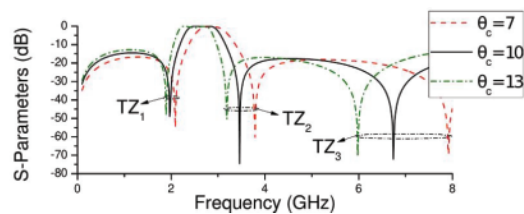**Figure 5:** Ideal response of the proposed single-band BPF
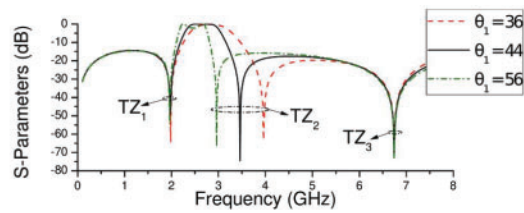
(a) Electrical length θ_1
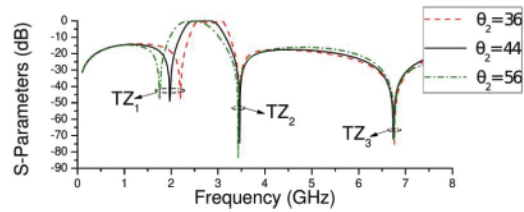
(b) Electrical length θ_2

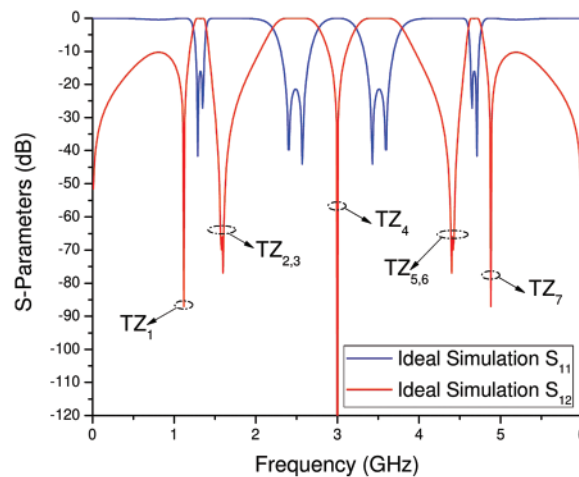(c) Electrical length θ_3

(d) Electrical length θ

Figure 6: Simulated results with tuning the electrical length

2.3 Proposed Quad-Band BPF Filter

The proposed quad-band BPF utilizes the same topology as of single-band BPF shown in Fig. 5; however, little modification in the electrical parameters of SRR and APCLS has been realized to obtain the dual-mode quad-band BPF response. Simulated results with tuning the electrical length

The extracted coefficient values are used to obtain the electrical parameters of the quad-band BPF. The obtained electrical parameter values are $Z_{in} = 84.7$, $\theta_{in} = 90$, $Z_1 = Z_2 = 128.6$ Ω, $\theta_1 = \theta_2 = 90$, $Z_e = 239.9$ Ω, $Z_o = 108.8$ Ω, $\theta_c = 90$, $Z_3 = 216.1$ Ω, $\theta_3 = 90$. The theoretical result of the quad-band BPF is given in Fig. 7, it can be seen that the eight transmission poles are achieved at $f_1 = 1.29$ GHz, $f_2 = 1.35$ GHz, $f_3 = 2.4$ GHz, $f_4 = 2.57$ GHz, $f_5 = 3.4$ GHz, $f_6 = 3.6$ GHz, $f_7 = 4.6$ GHz, and $f_8 = 4.7$ GHz . Moreover, seven finite frequency transmission zeros are obtained close to the passbands.


Figure 7: Ideal response of the proposed quad-band BPF

In order to further analyze the design topology, different electrical parameters are tuned, and the corresponding results are shown in Fig. 8. By changing the electrical length θ_1, θ_2, θ_3, θ_c the finite frequency transmission zeros and frequency band can be varied. The variation in the electrical length θ_1, θ_2, and θ_3 it is observed that the finite frequency transmission zeros can be varied toward the lower frequency and vice versa. Moreover, by changing the electrical length of the coupled line structure θ_c, the whole frequency band is being shifted.

(a) Electrical length θ_1

Figure 8: (Continued)

(b) Electrical length θ_2

(c) Electrical length θ_3
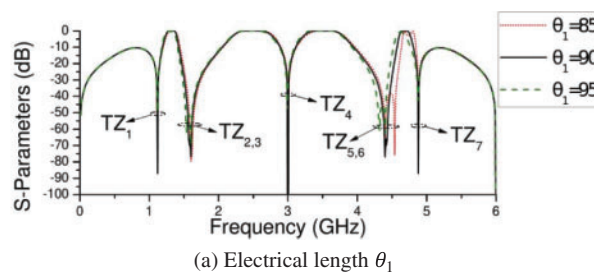
(d) Electrical length θ
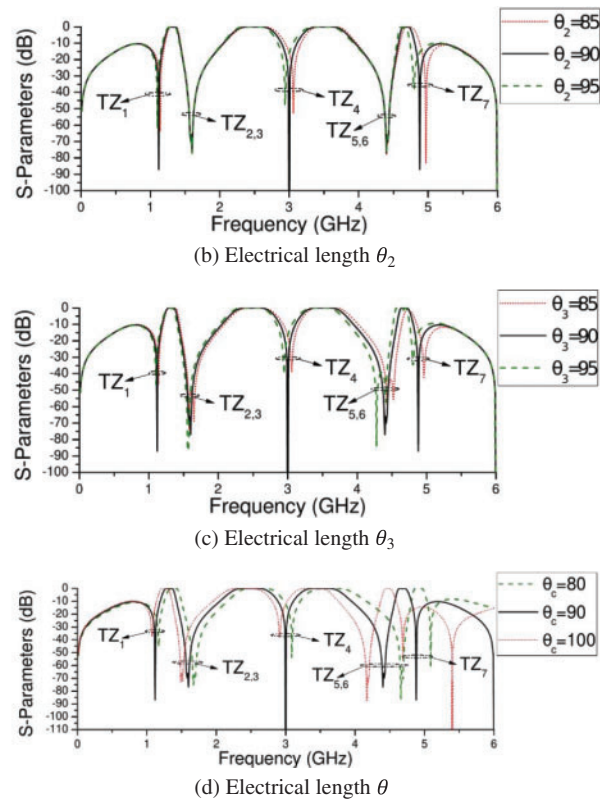
Figure 8: Simulated results with tuning the electrical length

## 3 Results and Discussion

For validation, the proposed single and quad-band BPF topologies are fabricated on Rogers Duroid 5880, and the measurements are done on Agilent N5242A PNA-X. The electrical parameters of both BPF filters are converted into their respective physical parameters using a line calculator, and the losses have been minimized using full-wave EM simulation.

The single-band BPF shown in Fig. 9 is labeled with optimized physical parameters at 2.65 GHz center frequency. The optimized physical parameters are $l_0 = 0.99$ mm, $l_1 = 11.01$ mm, $l_2 = 3.2$ mm, $l_3 = 8.61$ mm, $w_0 = 1.01$ mm, $w_1 = 0.41$ mm, $w_2 = w_3 = 0.88$ mm, $s = 0.2$ mm, and the size of the filter is $0.23\ \lambda_g \times 0.17\ \lambda_g$. The tapered line at the input and output are added to minimize the impedance mismatching.

Two transmission poles are measured at 2.48 GHz, and 2.68 GHz, as shown in Fig. 10. The 3 dB fractional bandwidth is measured to be 17.7% . The insertion loss for the measured results is less than 0.8 dB. Moreover, three finite frequency transmission zeros are measured at 2.2 GHz, 3.03 GHz, and 6.89 GHz having the rejection level of 31 dB, 39 dB, and 60 dB, respectively. The out of band rejection in the upper stopband region is above 16 dB up to 8 GHz. The little deviation of measured results compared to the simulated one is due to the limitation in fabrication and parasitic behavior of the SMA connectors. The measured group delay of the single band BPF is 1.9 ns at 2.65 GHz center frequency, as shown in Fig. 11.
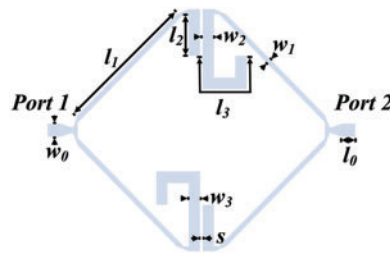
Figure 9: Top view of the single-band BPF filter
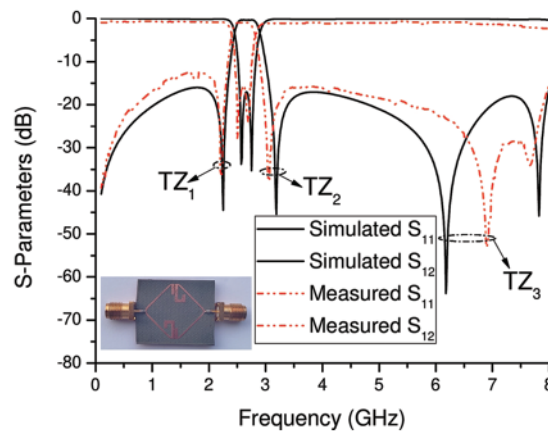
Figure 10: Simulated and measured results of fabricated single-band BPF
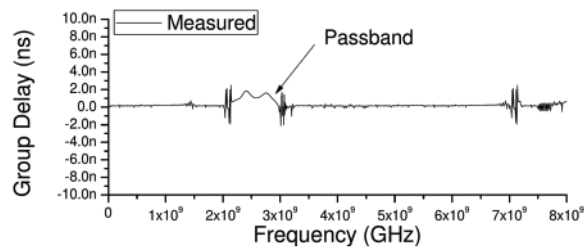
Figure 11: Measured group delay

The optimized electrical parameters of quad-band BPF filters is converted to physical parameters using a line calculator. The tuning and optimization is done to minimise the substrate losses. The optimized physical parameters labeled in Fig. 12 are $l_0 = 17.24$ mm, $l_1 = 17.20$ mm, $l_2 = 20.04$ mm, $l_3 = 17.76$ mm, $w_0 = 1.17$ mm, $w_1 = 0.68$ mm, $w_2 = 0.43$ mm, $w_3 = 0.43$ mm, $s = 0.2$ mm, and filter size is calculated to be $0.33 \lambda_g \times 0.36 \lambda_g$.

The comparison of microstrip simulated and measured results are shown in Fig. 13. Four passbands are measured, having center frequencies at 1.2 GHz, 2.4 GHz, 3.5 GHz, and 4.7 GHz, respectively. The 3 dB fractional bandwidth is measured to be 13%, 26%, 16%, and 5%, respectively. The measured insertion loss of all four passbands is less than 0.83 dB. The measured return loss for each passband is greater than 20 dB. Here it is worth mentioning that the proposed filter displays a dual-mode response for each passband. Moreover, seven transmission zeros around the four passbands have been measured at frequencies 1.01, 1.41, 1.47, 2.98, 4.29, 4.35, and 4.94 GHz. The rejection level of

all the transmission zeros is above 33 dB; whereas the rejection level of the transmission zeros between 1.4–1.6 GHz and 4.2–4.5 GHz is greater than 40 dB. The are some minor discrepancies seen in the measured response that is due to the input/output connectors mismatch. Fig. 14 displays the measured group delay of the four passbands. The maximum measured group delay at 1.2, 2.4, 3.5, and 4.7 GHz are 2.25, 1.2, 1.29, and 3.1 ns, respectively.
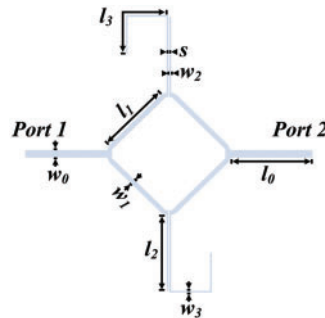
Figure 12: Top view of quad-band BPF
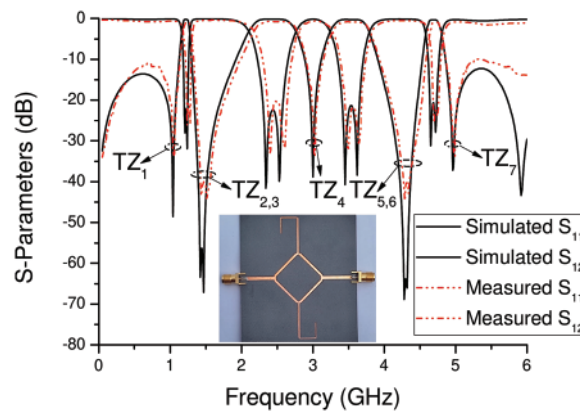
Figure 13: Measured and simulated results comparison
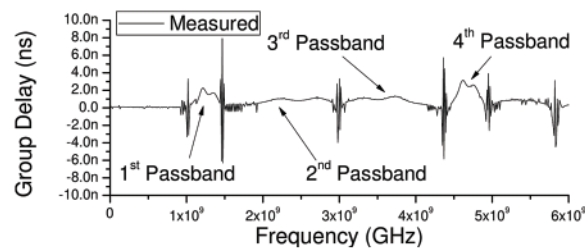
Figure 14: Measured group delay

Tab. 1 illustrates the comparison of the proposed single-band BPF with the previously reported work in the literature.

Tab. 2 shows the comparison of the proposed quad-band BPF with the reported ones. It can be seen from the table that the proposed filter provides better selectivity, low insertion loss, low to high fractional bandwidth, and higher out of band rejection.

Table 1: Comparison of the proposed single-band BPF with the reported filters

| Ref.	CFs (GHz)	IL (dB)	TZs	RL	FBW (%)	($\lambda_g \times \lambda_g$)
[1]	3	1	2	>11	66	0.23×0.07
[2]	3.9	0.85	4	>17	44	0.15×0.1
[5]	2.95	0.4	2	>20	77	0.12×0.23
[6]	5	1.87	2	>10	80	0.61×0.61
[7]	6.3	2.1	2	>12	108	0.4×0.27
[8]	4.5	1.6	1	>12	60	0.28×0.09
This work	2.65	0.8	3	>17	17	0.23×0.17

Table 2: Comparison of the proposed quad-band BPF with the reported filters

Ref.	CFs (GHz)	IL (dB)	TZs	RL	FBW (%)	($\lambda_g \times \lambda_g$)
[9]	1.5/2.5/3.6/4.6	1.98/1.74/3.58/3.4	3	>20/>17/>18/>20	5.5/12/11/4.3	0.3×0.3
[10]	1.57/1.8/2.5/2.65	1.1/1.3/1/1.2	7	>10/>10/>15/>12	7.6/8.3/5.7/3.7	0.3×0.25
[11]	1.46/2.6/4.5/5.25	1.5/1.9/1.7/2.0	4	>17/>20/>20/>19	8.6/4.5/5.2/4.2	0.14×0.12
[12]	0.94/2.27/3.55/5.66	0.41/2.06/1.77/1.73	6	>18/>14/>15/>15	40/15/22/13	0.13×0.1
[13]	2/2.7/3.45/4.55	1.6/1.6/1.3/1.5	5	>14/>12/>11/>15	7/7/6/6	0.18×0.28
[14]	1.9/2.8/4.3/5.2	2.3/3.6/3.5/3.4	3	>14/>20/>15/>19	5.3/3.4/3.5/3	0.44×0.25
[20]	2.4/3.5/5.2/5.8	1.8/1.5/2.1/2.9	6	>12/>20/>20/>20	6.8/6.1/3.1/1.4	0.23×0.23
[21]	1.57/2.45/3.5/5.2	0.78/1.45/2.3/1.42	2	>16/>12/>11/>13	6.9/3.4/2.9/4.7	0.2×0.3
This work	1.2/2.4/3.5/4.7	0.83/0.77/0.75/0.81	7	>21/>22/>23/>22	13/26/16/5	0.33×0.36

4 Conclusion

A split-ring resonator separated by an anti-parallel coupled line structure topology has been proposed to achieve single- and quad-band BPF. The synthesis procedure has been adopted to obtain the electrical parameters of the single and quad-band BPF. Moreover, the theory of the proposed topologies has been validated through the measured results of the fabricated prototypes. The calculated results of single- and quad-band BPF shows very low insertion loss in the passband and very high rejection in the lower and upper stopband regions. The proposed structures are suitable candidates for next-generation IoT wireless communication devices.

Conflicts of Interest: The authors declare that they have no conflicts of interest to report regarding the present work.

References

[1] H. N. Shaman, "New S-band bandpass filter BPF with wideband passband for wireless communication systems," *IEEE Microwave and Wireless Components Letters*, vol. 22, no. 5, pp. 242–244, 2012.

[2] K. Tanii and K. Wada, "Wideband bandpass filter composed of dual-path resonators using coupled-line and transmission line with inductive elements," *IEEE Microwave and Wireless Components Letters*, vol. 24, no. 1, pp. 14–16, 2013.

[3] H. Zhu and A. M. Abbosh, "Single-and dual-band bandpass filters using coupled stepped-impedance resonators with embedded coupled-lines," *IEEE Microwave and Wireless Components Letters*, vol. 26, no. 9, pp. 675–677, 2016.

[4] C. J. Chen, "A coupled-line coupling structure for the design of quasi-elliptic bandpass filters," *IEEE Transactions on Microwave Theory and Techniques*, vol. 66, no. 4, pp. 1921–1925, 2018.

[5] D. S. La, X. Guan, S. M. Chen, Y. Y. Li and J. W. Guo, "Wideband band-pass filter design using coupled line cross-shaped resonator," *MDPI Electronics*, vol. 9, no. 12, pp. 2173, 2020.

[6] A. Nakhlestani and A. Hakimi, "Wideband microstrip ring resonator bandpass filter with embedded rings," *Microelectronics Journal*, vol. 44, no. 5, pp. 462–467, 2013.

[7] D. Sarkar, T. Moyra and L. Murmu, "An ultra-wideband (UWB) bandpass filter with complementary split ring resonator for coupling improvement," *AEU-International Journal of Electronics and Communications*, vol. 71, no. 11, pp. 89–95, 2017.

[8] P. Zhang, L. Liu, D. Chen, M. H. Weng and R. Y. Yang, "Application of a stub-loaded square ring resonator for wideband bandpass filter design," *MDPI Electronics*, vol. 9, no. 1, pp. 176, 2020.

[9] J. Y. Wu and W. H. Tu, "Design of quad-band bandpass filter with multiple transmission zeros," *IET Electronics letters*, vol. 47, no. 8, pp. 502–503, 2011.

[10] B. Wu, F. Qiu and L. Lin, "Quad-band filter with high skirt selectivity using stub-loaded nested dual-open loop resonators," *IET Electronics Letters*, vol. 51, no. 2, pp. 166–168, 2015.

[11] L. Gao, X. Y. Zhang, X. L. Zhao, Y. Zhang and J. X. Xu, "Novel compact quad-band bandpass filter with controllable frequencies and bandwidths," *IEEE Microwave and Wireless Components Letters*, vol. 26, no. 6, pp. 395–397, 2016.

[12] L. Murmu and S. Das, "A compact quad-band bandpass filter using multi-mode stub-loaded resonator," *Progress In Electromagnetics Research Letters*, vol. 61, pp. 39–46, 2016.

[13] Q. Cao, H. Liu and L. Gao, "Design of novel compact quad-band bandpass filter with high selectivity," *De Gruyter Frequenz*, vol. 74, no. 1–2, pp. 53–59, 2020.

[14] J. Xu, C. Miao, L. Cui, Y. X. Ji and W. Wu, "Compact high isolation quad-band bandpass filter using quad-mode resonator," *IET Electronics Letters*, vol. 48, no. 1, pp. 28–30, 2012.

[15] X. Li, Y. Zhang, Y. Tian, Y. Yang and Y. Fan, "Quad-and sext-band bandpass filter based on multimode resonator utilizing SIRs-loaded tapered-line," *Microwave and Optical Technology Letter*, vol. 60, no. 3, pp. 650–654, 2018.

[16] Q. Yang, Y. C. Jiao and Z. Zhang, "Compact multiband bandpass filter using low-pass filter combined with open stub-loaded shorted stub," *IEEE Transactions on Microwave Theory and Techniques*, vol. 66, no. 4, pp. 1926–1938, 2018.

[17] Z. Li, L. Wang, M. He, X. Li, Z. Liang *et al.,* "Compact dual-/tri-/quad-band bandpass filters with independently frequency-tunable and switchable passbands," *International Journal of Microwave and Wireless Technologies*, vol. 13, no. 4, pp. 322–334, 2021.

[18] D. K. Choudhary and R. K. Chaudhary, "Miniaturized quad-band filter with improved selectivity using split ring resonators and metallic strips," *International Journal of RF and Microwave Computer-Aided Engineering*, vol. 31, no. 10, pp. e22809, 2021.

[19] J. Zhang, Q. Liu, D. W. Zhang and Y. Qu, "High selectivity single wideband and quad-band HTS filters using novel quad-mode resonators with self-coupled structure," *IEEE Access*, vol. 9, pp. 103194–103203, 2021.

[20] J. Wang, S. He and D. Gan, "A 2.4/3.5/5.2/5.8-GHz quad-band BPF using SLRs and triangular loop resonators," *IET Electronics Letters*, vol. 54, no. 5, pp. 299–301, 2018.

[21] F. Wei, Q. Huang, X. H. Wang, W. T. Li and X. W. Shi, "Compact step-impedance ring resonator for quad-band band-pass filter," *Progress In Electromagnetics Research Letters*, vol. 41, pp. 105–112, 2013.

[22] X. R. Zhang, X. Sun, W. Sun, T. Xu and P. P. Wang, "Deformation expression of soft tissue based on BP neural network," *Intelligent Automation & Soft Computing*, vol. 32, no. 2, pp. 1041–1053, 2022.

[23] J. Zhang, Z. Wang, Y. Zheng and G. Zhang, "Design of network cascade structure for image super-resolution," *Journal of New Media*, vol. 3, no. 1, pp. 29–39, 2021.

[24] G. I. Zysman and A. K. Johnson, "Coupled transmission line networks in an inhomogeneous dielectric medium," *IEEE Transactions on Microwave Theory and Techniques*, vol. 17, no. 10, pp. 753–759, 1969.

[25] S. Khalid, W. Peng Wen and L. Yen Cheong, "Optimum filter synthesis procedure for ultra-wideband bandpass filter using step-impedance resonator," *Journal of Electromagnetic Waves and Applications*, vol. 28, no. 8, pp. 943–955, 2014.

[26] M. Faisal, S. Khalid, M. U. Rehman and M. A. Rehman, "Synthesis and design of highly selective multi-mode dual-band bandstop filter," *IEEE Access*, vol. 9, pp. 43316–43323, 2021.